OPEN ACCESS

Biomedicine ARTICLE

The Innovation Oncology

Multiview classification of pediatric medulloblastoma refines prognostic stratification and enables imaging-based risk prediction

Adam Kraya,[1,2,8,*] Komal Rathi,[1,2] Anahita Fathi Kazerooni,[1,2,5] Ammar S. Naqvi,[1,2] Ariana M. Familiar,[1,2] Yiran Guo,[1,2] Qi Li,[1,2] Varun Kesherwani,[1,2] Angela N. Viaene,[3,4] Mariarita Santi,[3,4] Deep Gandhi,[2] Yuankun Zhu,[1,2] Xiaoyan Huang,[1,2] Bo Zhang,[1,2] Arastoo Vossough,[2,7] Ali Nabavizadeh,[1,2,7] Phillip B. Storm,[1,2] Adam C Resnick,[1,2] and Brian R. Rood[6,8,*]

*Correspondence: krayaa@chop.edu (A.K.); brood@childrensnational.org (B.R.R)

Received: February 28, 2026; Accepted: July 2, 2026; Published Online: July 10, 2026; https://doi.org/10.59717/j.xinn-oncol.2026.100025

GRAPHICAL ABSTRACT

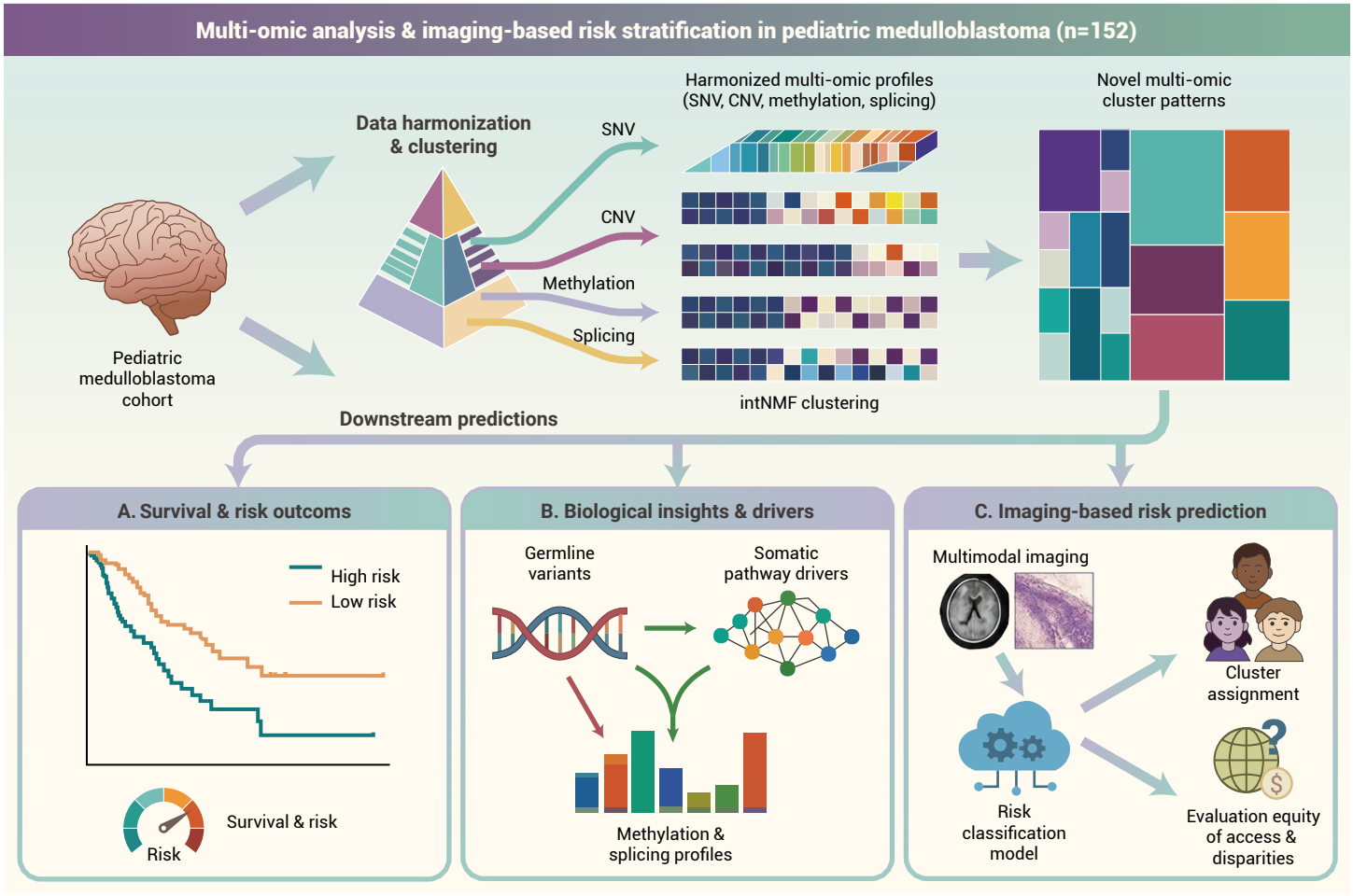

PUBLIC SUMMARY

- We developed novel multiomic classifications for pediatric medulloblastoma to improve risk stratification.
- 14 distinct molecular clusters reveal high- and low-risk populations that were previously grouped together.
- Magnetic resonance and pathology images can predict molecular risk groups, improving accessibility.
- This model offers a path toward reducing toxic drug effects and improving survival for aggressive disease.

ARTICLE Biomedicine

OPEN ACCESS

Multiview classification of pediatric medulloblastoma refines prognostic stratification and enables imaging-based risk prediction

Adam Kraya,[1,2,8,*] Komal Rathi,[1,2] Anahita Fathi Kazerooni,[1,2,5] Ammar S. Naqvi,[1,2] Ariana M. Familiar,[1,2] Yiran Guo,[1,2] Qi Li,[1,2] Varun Kesherwani,[1,2] Angela N. Viaene,[3,4] Mariarita Santi,[3,4] Deep Gandhi,[2] Yuankun Zhu,[1,2] Xiaoyan Huang,[1,2] Bo Zhang,[1,2] Arastoo Vossough,[2,7] Ali Nabavizadeh,[1,2,7] Phillip B. Storm,[1,2] Adam C Resnick,[1,2] and Brian R. Rood[6,8,*]

[1]Division of Neurosurgery, The Children's Hospital of Philadelphia, Philadelphia 19104, USA
[2]Center for Data-Driven Discovery in Biomedicine (D3b), The Children's Hospital of Philadelphia, Philadelphia 19104, USA
[3]Department of Pathology and Laboratory Medicine, The Children's Hospital of Philadelphia, Philadelphia 19104, USA
[4]Department of Pathology and Laboratory Medicine, University of Pennsylvania, Philadelphia 19104, USA
[5]Department of Neurosurgery, Perelman School of Medicine, University of Pennsylvania, Philadelphia 19104, USA
[6]Brain Tumor Institute, Children's National Research Institute, Washington DC 20010, USA
[7]Department of Radiology, University of Pennsylvania, Philadelphia 19104, USA
[8]These authors contributed equally
*Correspondence: krayaa@chop.edu (A.K.); brood@childrensnational.org (B.R.R)

Received: February 28, 2026; Accepted: July 2, 2026; Published Online: July 10, 2026; https://doi.org/10.59717/j.xinn-oncol.2026.100025

Citation: Kraya A., Rathi K., Kazerooni A. F., et al. (2026). Multiview classification of pediatric medulloblastoma refines prognostic stratification and enables imaging-based risk prediction. *The Innovation Oncology* **1**:100025.

Despite advances in molecular subclassification, significant heterogeneity within the four primary medulloblastoma subgroups complicates therapeutic design. High-risk SHH and Group 3/4 cases, particularly those with metastases, frequently fail conventional therapy, highlighting the urgent need for molecularly-based risk refinement and improved disease estimation. By integrating five distinct molecular layers—non-synonymous variants, copy number variations (CNVs), DNA-methylation, gene expression, and alternative splicing—we identified 14 multi-omic clusters (MOCs) across 152 primary tumors from the Children's Brain Tumor Network (CBTN). Within Group 3, we identified two prognostically distinct MOCs (p = 0.00024); favorable outcomes were linked to high-fidelity genomic maintenance and proteostasis, while poor prognosis was characterized by Notch signaling and metabolic reprogramming (*IDH2/3B*). Similarly, Group 4 MOCs showed divergent outcomes (p = 0.039) driven by either RTK-mediated proliferation or epigenetic stability. Germline analysis revealed that chromatin-modifying variants (*SIRT2*, *PRDM2*) associated with favorable clusters, while invasion-associated variants (*PTPRT*, *EPHA1*) linked to tumor aggression. In an effort to explore potential avenues for clinical translation, we modeled MRI and histopathology features as surrogates for these molecularly-defined risks. This integrated multi-omic approach refines our understanding of medulloblastoma outcomes, suggesting that integrated omics coupled with clinical imaging can significantly enhance precision medicine and prognostication.

INTRODUCTION

Medulloblastoma (MB) is the most prevalent malignant pediatric brain tumor, and despite aggressive intervention, relapses yield survival rates below 5%.[1] For decades, the standard of care (surgery, craniospinal radiation, and intensive chemotherapy) has remained largely stagnant. While these multimodal approaches have improved survival, they impose a devastating toll on survivors. Recent population-based studies demonstrate that 5-year survivors face a 21-fold increase in mortality and a 45-fold increase in stroke risk compared to healthy controls, with nearly half of all survivors requiring permanent disability support.[2] These long-term sequelae, including severe neurocognitive deficits and endocrine dysfunction, significantly diminish the quality of life for pediatric patients.[3,4]

The 2021 WHO classification identifies four molecular subgroups: WNT, SHH, Group 3, and Group 4.[4] Although second-generation efforts utilizing RNA-seq and methylation profiling have revolutionized diagnostic workflows, they have yet to successfully translate into precision medicine combination therapies.[5] Current clinical frameworks often fail to resolve the latent biological heterogeneity within these subgroups, and uniform treatment protocols remain the norm. While recent clinical trials like SJMB12 have begun to explore risk-adapted therapy reduction for low-risk WNT tumors,[6] there remains an urgent unmet need for stratified therapeutic approaches for the more aggressive G3/4 tumors to reduce systemic toxicity while improving outcomes.[1,7]

Progressively building on these existing subtyping efforts, our study introduces an integrated five-layer multi-omic model. By leveraging non-synonymous variants, copy number variations, DNA methylation, gene expression, and uniquely alternative splicing, we identified 14 Multi-Omic Clusters (MOCs) across 152 primary tumors from the Children's Brain Tumor Network (CBTN), demonstrating deep biological and prognostic distinctions. Recognizing that comprehensive multi-omic profiling is not globally accessible, we evaluated the feasibility of bridging the gap between molecular biology and clinical imaging data. We developed a predictive framework using MRI and digitized H&E histopathology features to estimate molecularly-derived risk. While these imaging-based findings represent a preliminary step, they suggest a path toward equitable access to precision stratification. Collectively, this work provides a granular biological map of medulloblastoma, nominating novel putative therapeutic targets and druggable pathways to guide future combination therapies and improve prognostication.

MATERIALS AND METHODS

Data processing

Processing of genomic, transcriptomic, and methylation data, including methods for feature selection, can be found under Supplementary Methods. To account for multiple hypothesis testing for differential pathway expression (2.2), differential methylation analysis (2.3) and LINCS analysis (identification of reversers and pathways related to reversers), we leveraged a false discovery rate (FDR) threshold of 0.05 for all tests. For survival analyses by log-rank tests and Cox regression analyses, test statistics with p-values of 0.05 or less were considered significant.

Somatic variant analysis and visualization

See Supplementary Methods.

IntNMF clustering

To perform an integrative clustering analysis using multiple types of genomic datasets, we used the IntNMF (Integrative Non-negative Matrix Factorization) R package.[8] Please see Supplementary Methods for a complete description of model derivation and validation.

Post clustering associations

Survival analysis. Survival outcomes for the CBTN medulloblastoma were evaluated under three independent conditions: a) when annotated according to their MOC, b) when annotated according to an in-house RNA-based supervised classifier that categorizes medulloblastoma tumors into one of four major WHO 2021 subtypes,[4] and c) when annotated according to second-generation methylation subtypes (DKFZ[9]). Please see Supplementary Methods for a complete description of survival modeling.

Pathway-based analysis. Whole transcriptome and methylation data were batch-corrected and evaluated for differential pathway expression (see Supplementary Methods).

Identification of putative regulatory methylation sites. MethylMix was used to identify putative regulatory methylation sites, we leveraged the MethylMix Bioconductor packages[10] (see Supplementary Methods).

Analysis of Cluster-Specific Germline Variants. The rates of potentially deleterious germline mutations were evaluated across MOCs using an in-house bioinformatic pipeline (see Supplementary Methods).

LINCS analysis. For each MOC, DEGs were leveraged within the Library of Integrated Network-Based Cellular Signatures (LINCS) analysis framework for identifying potentially targetable biological pathways (see Supplementary Methods).

Identification of Survival-Associated Splicing Variants. To identify alternative splicing events associated with overall survival in medulloblastoma subgroups, we leveraged percent spliced-in (PSI) values from rMATS in combination with Cox regression and differential weighting by intNMF (see Supplementary Methods).

Imaging-based machine learning models

Magnetic resonance imaging (MRI) data processing. MRI (mpMRI) data were collected for 133 subjects, including pre- and post-contrast T1-weighted (T1w, T1w-Gd), T2-weighted (T2w), T2 fluid-attenuated inversion recovery (T2-FLAIR), and diffusion-weighted imaging (DWI). Full details regarding radiomic feature extraction can be found in Supplementary Methods.

Digitized H&E slide data processing. Available whole-slide histopathology images (WSIs) of the formalin-fixed paraffin-embedded (FFPE) slides were collected from the public CBTN data repository, corresponding to tumor biospecimen samples used for molecular sequencing. Full details can be found in Supplementary Methods.

Machine learning analysis for imaging-based prediction of MOC-defined risk. To evaluate the ability of imaging and pathomics features to predict risk in medulloblastoma, we re-partitioned our medulloblastoma cohort into low, intermediate-low, intermediate-high, and high-risk groups based on the quartiles of risk scores computed from the MOC-based Cox regression model described in supplementary methods. Full details can be found in Supplementary Methods.

RESULTS

Demographic and clinical characteristics of the CBTN medulloblastoma cohort

With multi-omic data from molecular profiling of 152 primary medulloblastoma tumors from the CBTN, we hypothesized that genomic, epigenomic, and transcriptomic data would jointly improve the resolution of medulloblastoma subtypes, with the potential of improving risk stratification and uncovering novel disease biology (Figure 1A). Our cohort consisted primarily of Group 4 (G4, 43%), followed by Group 3 (G3, 23.4%), Sonic Hedgehog (SHH, 22.2%), and WNT subgroups (Figure S1A, 11.4%), consistent with global pediatric medulloblastoma epidemiological characteristics.[6,11] 61% of the study participants were male, and 70% of the participants had gross total resection, compared to 27% with partial resection and 2.6% for which only a biopsy was performed (Table S1). More than 90% of patients received chemotherapeutic treatment and approximately 80% received craniospinal radiation (Table S1).

When considering WHO-based and second generation DFKZ methylation-based classifications of this tumor cohort, we observed rare instances of WHO subgroups mapping to control tissue from second-generation methylation subtyping (unlabeled ticks, Figure S1A). When evaluating subgroup-specific clinical events, more than 70% of SHH and 89% of WNT tumors (16/18) did not experience recurrence or progression, in contrast to 51% for G3 tumors and 68% for G4 tumors. With respect to overall survival, 67.5% of SHH, 75.7% of G4, and 94.7% of WNT tumor cases were alive at the time of last follow-up, in contrast to 54.5% of G3 tumors (Figure S1B).

Clinical prognostication of medulloblastoma multi-omic clusters (MOCs)

Single-nucleotide variant (SNV)/indel, CNV, RNA-Seq, splicing (percent splice inclusion, PSI values), and methylation array data were provided as input to intNMF. 100 random initializations of the algorithm illustrated high clustering quality and stability (Figure 1B), evidenced by a high cophenetic correlation of 0.98, dispersion of 0.93, and average silhouette index of 0.78 (Figure 1C). When comparing WHO classifications to our MOC model (Table 1, Figure 2A), we found that WNT tumors remained a relatively pure MOC (MOC4, n=17) and SHH tumors largely bifurcated into two major MOCs (2 and 5, n=18 and n=8, respectively), while also subclustering to a minor extent to MOCs 3, 7, and 14 (n=9, n=4, n=4, respectively). However, more complex subclustering was observed for G3/4 tumors, particularly when evaluating second generation DKFZ subtypes. Notably, MOCs 9 (n=16) and 10 (n=9), both G3 tumor clusters, were comprised of subsets of second-generation G3/4_III and G3/4_IV for the former and a subset of G3/4_III with a pure group of G3/4_II for the latter (Table 1, Figure 2B). G4 tumors clustered into 4 MOCs, 2 of which represented pure subsets of second generation G3/4 subtypes (MOC6: G3/4_VII and MOC13: G3/4_VIII; n=17 and n=21, respectively). The MOCs 8 (n=8) and 12 (n=15), also mapping to G4, contained tumors from multiple subtypes including G3/4_V, VI, VII, VIII.

When comparing overall survival (OS) by Kaplan-Meier (KM) analysis, we found that the outcomes across the 14 MOC subtypes differed highly significantly ($p < 0.0001$, log-rank test, Figure 2C). When annotating our CBTN cohort with WHO 2021 subgroups, there was non-significant evidence of an association with OS outcomes ($p = 0.055$, 2D) and significant evidence of association between DKFZ classifications and OS outcomes (p=0.013, Figure 2E). By Cox regression analysis, OS was also significantly worse for MOCs 10 ($p < 0.001$, n=9), 12 ($p < 0.001$, n=15), and 13 ($p = 0.025$, n=21) in addition to MOC9 by Cox regression analysis (G3, $p < 0.001$, n=16, Figure 2F). However, among G3 MOC's, the observed OS hazard ratio (HR) for MOC10 (HR = 26.8, n=9) was substantially higher than that of MOC9 (HR = 3.15, n=16, Figure 2F). A KM comparison between MOC's 9 (n=16) and 10 (n=9) demonstrated a significant difference in OS outcomes between these two G3 subclusters ($p = 0.00024$, Figure 2F), visually underscoring a difference in survival outcomes among these two G3 MOCs; notably, metastatic status, rates of radiation treatment, and rates of chemotherapy treatment were similar across MOCs 9 (metastasis: 5 of 16 tumors; radiation: 13 of 16 tumors; chemotherapy: 16 of 16 tumors) and 10 (metastasis: 3 of 9 tumors; radiation: 6 of 9 tumors; chemotherapy: 9 of 9 tumors). Differences between G4 MOCs were also evident by KM (Figure 2F), whereby MOCs 8 (metastasis: 3 of 8 tumors; radiation: 8 of 8 tumors; chemotherapy: 8 of 8 tumors) and 13 (metastasis: 5 of 16 tumors; radiation: 13 of 16 tumors; chemotherapy: 16 of 16 tumors) had significantly longer OS than MOCs 6 (metastasis: 5 of 17 tumors; radiation: 15 of 17 tumors; chemotherapy: 17 of 17 tumors) and 12 (metastasis: 4 of 21 tumors; radiation: 19 of 21 tumors; chemotherapy: 19 of 21 tumors), also with similar rates of metastasis, radiation treatment, and chemotherapy treatment. These results suggest that multi-omic clustering provides an additional layer of prognostic resolution, identifying distinct survival trajectories within G3 and G4 cohorts in particular.

Neither the WHO, DKFZ, or MOC models resulted in significant differences based on event-free survival (EFS) outcomes by KM analysis, though there was evidence of an association for the latter ($p = 0.06$, Figures 3A-C). When evaluating EFS in a Cox regression model adjusting for age and extent of resection, we observed significantly worse EFS for MOCs 10 (G3, $p < 0.001$, n=9), 12 (G4, $p < 0.001$, n=15), and 13 (G4, $p = 0.02$, n=21), but not MOC9 (n=16), when using WNT-driven MOC cluster 4 as the reference group (Figure 3D).

Independent validation of medulloblastoma MOC model

We tested the robustness of our MOC assignments by projecting them onto an independent cohort (Cavalli et al).[3] This required bridging significant platform gaps, most notably the transition from five omic layers in the discovery phase (including RNA-seq-derived splicing and EPIC v1 methylation) to a two-layer validation using legacy 450k methylation and expression microarray data. The inability to incorporate alternative splicing, genomics, or high-density EPIC probes in the validation set resulted in a drastically reduced feature set (583 CpGs; 909 transcripts). Despite this reduction in multi-omic depth and feature density, the distribution of WHO 2021 subgroups across MOC classifications in the Cavalli cohort largely recapitulated the discovery findings (Table S2). Notably, MOC2 (100% SHH), MOC4 (100% WNT), MOC5

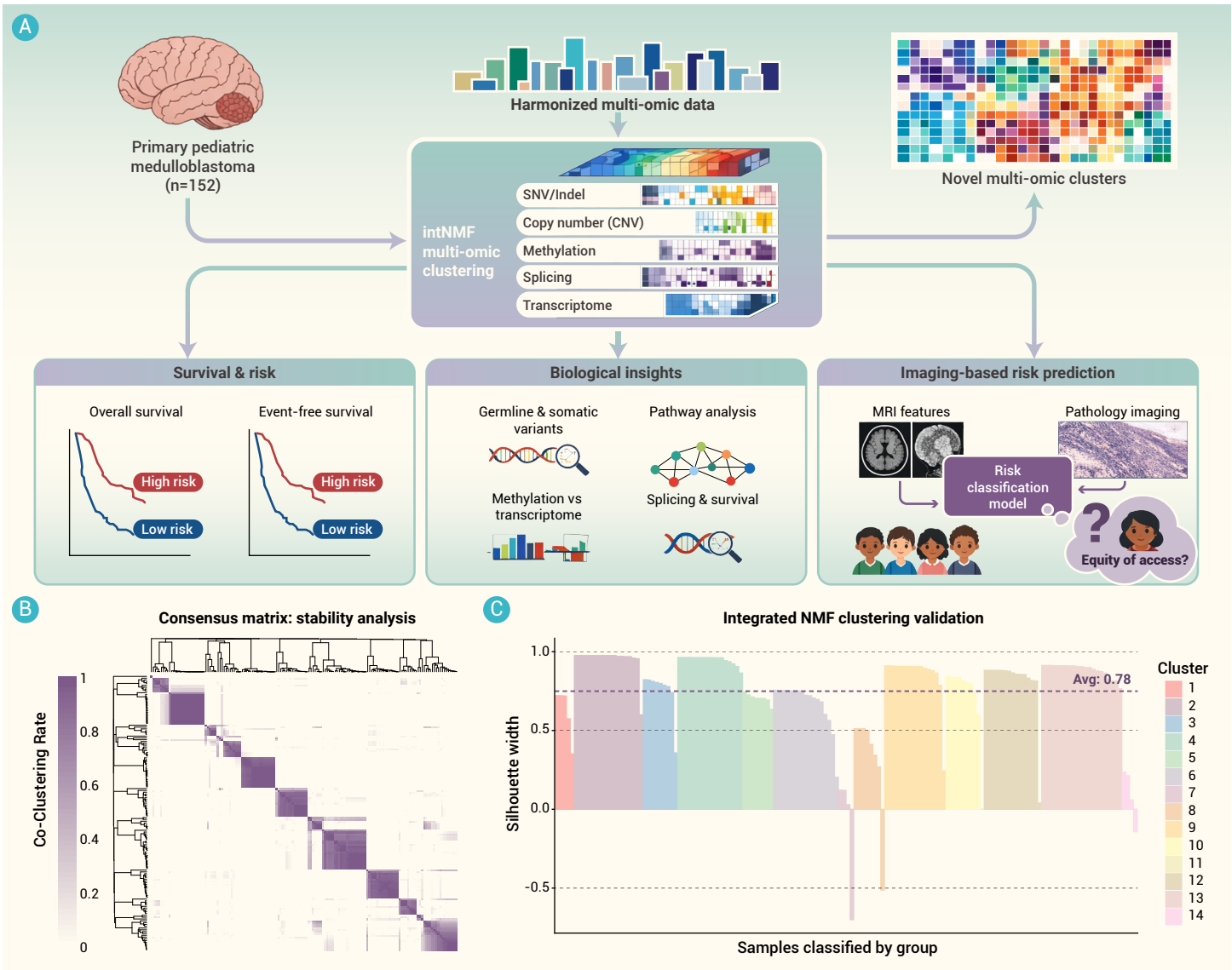

Figure 1. Multi-omic clustering strategy and quality assessment of multi-omic clusters (MOCs) (A) High-level schematic of multi-omic clustering strategy and downstream characterization for primary medulloblastoma tumors of the CBTN. (B) Pairwise co-clustering frequency matrix illustrating MOC stability from random initializations of the intNMF multi-omic clustering algorithm. (C) Graphical representation of per-sample clustering quality from multi-omic clustering quantified by the silhouette index.

(96% SHH), and MOCs 8, 10, and 13 (100% G4, G3, and G4, respectively) exhibited high subgroup purity, consistent with the original model. Also consistent with the discovery model, MOCs 1, 6, and 12 remained predominantly G4 (>90%). Minor shifts were observed in MOC9, which displayed a predominantly G3 composition (83%) in the validation cohort compared to the purely G3 discovery profile. MOC3 retained its characteristic heterogeneous mix of Group 3, G4, and SHH tumors.

Survival analysis was conducted to determine if the MOC framework maintained its prognostic utility in the independent validation cohort. In line with the discovery cohort, G3-associated MOCs 9 and 10 demonstrated significantly different outcomes; Kaplan-Meier analysis confirmed that MOC9 was associatedwith a favorable overall survival (OS) relative to the poorer outcomes observed in MOC10 (log-rank p = 0.032, Figure S2A). For the G4-associated MOCs (6, 8, 12, and 13), the prognostic trends observed in the discovery cohort were partially conserved. While the four-way comparison did not reach statistical significance via log-rank test (p = 0.16, Figure S2B), pairwise comparisons between MOC12 and 13 showed evidence of an association between OS and MOC cluster (weighted log-rank p = 0.08, unweighted log-rank p = 0.099, Figure S2C), with MOC13 exhibiting the more favorable OS, consistent with the CBTN model.

When performing Cox regression in the Cavalli dataset, adjusting for age group and using the WNT-specific MOC4 as the reference (Table S3), reinforced the discovery findings, as both MOC9 and MOC10 were associated with significantly higher hazards of failure compared to the WNT reference, with MOC10 exhibiting a markedly higher hazard (β = 10.2, p = 0.00027) than MOC9 (β = 6.4, p = 0.0027). Among G4 MOCs, survival patterns showed similar trends to the discovery cohort; MOC6 (β = 5.19, p=0.010) and MOC12 (β = 7.6, p = 0.00082) demonstrated increased hazards of failure, whereas MOC13 presented a relatively lower hazard (β = 4.52, p = 0.015) compared to MOC's 6 and 12. These conserved patterns occurred despite the reduction in the feature space in Cavalli data relative to CBTN data, as well as the multicenter, international nature of the Cavalli dataset. Further, differences in global treatment standards and follow-up rigor across several decades introduce a level of heterogeneity not present in our CBTN discovery cohort, potentially impacting global survival significance by KM analysis.

Collectively, these findings suggest that the intNMF-derived MOC framework identifies biologically and clinically relevant sub-populations of medulloblastoma that persist across different patient cohorts and profiling technologies.

Investigation of germline variants in prognostically significant MOCs

We analyzed the germline variant landscape, focusing on prognostically distinct G3/4 MOCs given the historic challenges in identifying novel treatment approaches for these medulloblastoma subtypes.[12] We identified 28 of such germline variants among the cohort of 152 patients (Table S4) through

Table 1. Relationships between MOC's, WHO 2021 CNS tumor classification, and DKFZ methylation-based classifications.

Alignment of Medulloblastoma Classification Systems Summary of WHO and DKFZ groupings mapped by MOC assignment		
Multi-Omic Cluster (MOC)	**WHO 2021 CNS Classification**	**DKFZ (Heidelberg) Methylation Classification**
MOC1	MB, Group3, MB, Group4, MB, WNT	MB_G34_III, MB_G34_IV, MB_G34_VII
MOC2	MB, SHH	MB_SHH_1, MB_SHH_2, MB_SHH_3, MB_SHH_4
MOC3	MB, Group3, MB, Group4, MB, SHH	MB_G34_VI, MB_G34_VII, MB_MYO, MB_SHH_2
MOC4	MB, WNT	MB_WNT
MOC5	MB, SHH	MB_SHH_1, MB_SHH_2, MB_SHH_3
MOC6	MB, Group4	MB_G34_VII
MOC7	MB,Group3, MB, Group4, MB, SHH	MB_G34_I, MB_G34_V, MB_SHH_4
MOC8	MB, Group4	MB_G34_V, MB_G34_VI, MB_G34_VII, MB_G34_VIII
MOC9	MB, Group3	MB_G34_II, MB_G34_III, MB_G34_IV, MB_G34_VII
MOC10	MB, Group3	MB_G34_II, MB_G34_III, MB_G34_V
MOC11	MB, Group3	MB_G34_III
MOC12	MB, Group4	MB_G34_V, MB_G34_VII, MB_G34_VIII
MOC13	MB, Group4	MB_G34_VIII
MOC14	MB, Group3, MB, SHH	MB_G34_III, MB_SHH_1

a Bayesian point-based system of ACMG-based classification.[13,14]

In the analysis of G3 tumors, MOC9 mapped to an individual with a Tier-I pathogenic stop-gain variant in *PRDM2* (p.Trp76Ter), which encodes a histone methyltransferase that functions as a tumor suppressor whose inactivation can contribute to medulloblastoma pathogenesis.[15] Notably, WNT and specific G3/4 subtypes driven by epigenetic dysregulation may respond better to therapy than those driven by structural alterations.[16] Conversely, individuals within MOC10 (n=9) contained variants in genes associated with invasion and aggressive cell signaling (Table S4). Notable Tier-I findings included a variant in *PTPRT* (p.Arg999Ter) and a variant in *EPHA1* (p.Leu399ProfsTer58). *PTPRT* loss, observed here via a nonsense mutation, can lead to constitutive STAT3 activation that can enhance tumor cell survival, proliferation, and metastasis in high-risk brain tumors.[17] Similarly, *EPHA1* belongs to the ephrin receptor subfamily, which regulates cell adhesion and migration and whose dysregulation is a hallmark of the metastatic nature characteristic of aggressive G3 medulloblastoma.[18]

G4 tumors showed differences in germline mutations between favorable (MOCs 8 & 13, n=8 and n=21) and intermediate (MOCs 6 & 12, n=17 and n=15) prognostic groups. The favorable prognosis subgroup MOC13 (n=21) included a frameshift mutation in *SIRT2* (p.Ser27Ter), an NAD+-dependent deacetylase (Table S4) whose disruption may sensitize tumors to DNA-damaging agents used in standard adjuvant therapy.[19] The identification of this chromatin-modifying germline variant in the favorable G4 MOC reinforces the hypothesis that G4 tumors are driven by epigenetic instability, which may represent a therapeutic vulnerability. By contrast, the intermediate prognosis subgroup MOC12 (n=15) was characterized by a heterogeneous set of variants in large neurodevelopmental genes, including *RGS7* and *THBS2*. *RGS7* is highly expressed in the cerebellum and regulates G-protein signaling, and *THBS2* is involved in synaptogenesis.

Collectively, these data, while limited in number, suggest that germline predisposition may be related to the molecular trajectory of medulloblastoma subtypes. The segregation of chromatin modifiers (*SIRT2*, *PRDM2*) into favorable prognostic clusters, contrasted with invasion-associated signaling variants (*PTPRT*, *EPHA1*) in poor prognostic clusters, supports a model where the germline background may influence tumor aggression.

Analysis of somatic chromosomal copy number variation within MOCs

We evaluated differences in the rates of arm-level somatic copy number variants (CNVs) across the MOCs, modeling the counts by Poisson generalized linear models (GLMs), adjusting for cluster size and specifying WNT MOC4 as the reference cluster. We observed significantly higher rates of chr17p changes in G4 MOCs 6 (ß = 2.39, p.adj = 0.041 (FDR-adjusted), n=17), 8 (ß = 2.67, p.adj = 0.029, n=8), 12 (ß = 2.59, p.adj = 0.029, n=15), and 13 (ß = 2.76, p.adj = 0.029, n=21, Figure 4A). Among nominally significant events (nominal p-value < 0.05) with adjusted p-values greater than 0.1, we observed higher rates of chr17q alterations in MOC12 (G4, ß = 2.31, p = 0.021, p.adj = 0.155, n=15) and MOC13 (G4, ß = 2.48, p = 0.013, p.adj = 0.155, n=21). Higher rates of chr8p alterations were observed in MOC1 (G3/4 + WNT, ß = 2.21, p = 0.027, p.adj = 0.151, n=5) and MOC6 (G4, ß = 2.08, p = 0.038, p.adj = 0.151, n=17). When modeling the probability of ichr17 occurrence via binomial regression, we found that MOCs 1 (G3/4 + WNT, ß = 3.18, p = 0.021, n=5), 8 (G4, ß = 2.77, p = 0.027, n=8), 12 (G4, ß = 3.47, p = 0.003, n=15), and 13 (G4, ß = 3.94, p = 0.00063, n=21) in particular were associated with significantly higher rates of ichr17.

The concentration of 17p loss and isochromosome 17q (i17q) within specific G4 MOCs (MOCs 8, 12, and 13, but not MOC6), a prevalent G4 structural hallmark,[1,15] indicates that multi-omic integration can further partition the known intertumoral heterogeneity of G4 into biologically distinct states.[3] Furthermore, the observation of 8p loss and mostly isolated 17p changes in the absence of ichr17q within MOC6 provides early indications of a distinct trajectory for this G4 subset, where the loss of localized tumor suppressor loci on this arm may be a driver of its less favorable observed outcome.[5]

Biological characterization of MOC4 (WNT) tumors

To understand the biology of our MOCs, we evaluated the most heavily weighted features from intNMF (Table S5, Figure 4B). Focusing on SNVs, insertion-deletion events (indels), and CNVs (Table S5A-B), we found that *CTNNB1*, *DDX3X*, and *TP53* were the most frequently mutated genes in MOC4 (n=17, Figure 3B), comprised solely of WNT-driven tumors. Further, the general themes of disruption in chromatin and transcriptional regulation (*KMT2C, KMT2D, DOT1L, KDM6A*), cell cycle control (*TP53, SOX4, FOXM1, MYBL1*), and cell adhesion and ECM remodeling (Tables S5A-B) emerged as the most prevalent. At the transcriptional level, differentially expressed pathways (DEPs) included amino acid metabolic and transport pathways, cellular response to starvation, and collagen biosynthesis when comparing to the rest of the tumor cohort (Figure S3A). Differentially methylated pathways (DMPs) included those related to extracellular matrix (ECM) reorganization, G-protein coupled receptor (GPCR) signaling, and receptor tyrosine kinase (RTK) signaling (Figure S4A). Furthermore, we found biological mechanisms that were prevalent at the genomic level, namely chromatin regulation and cell

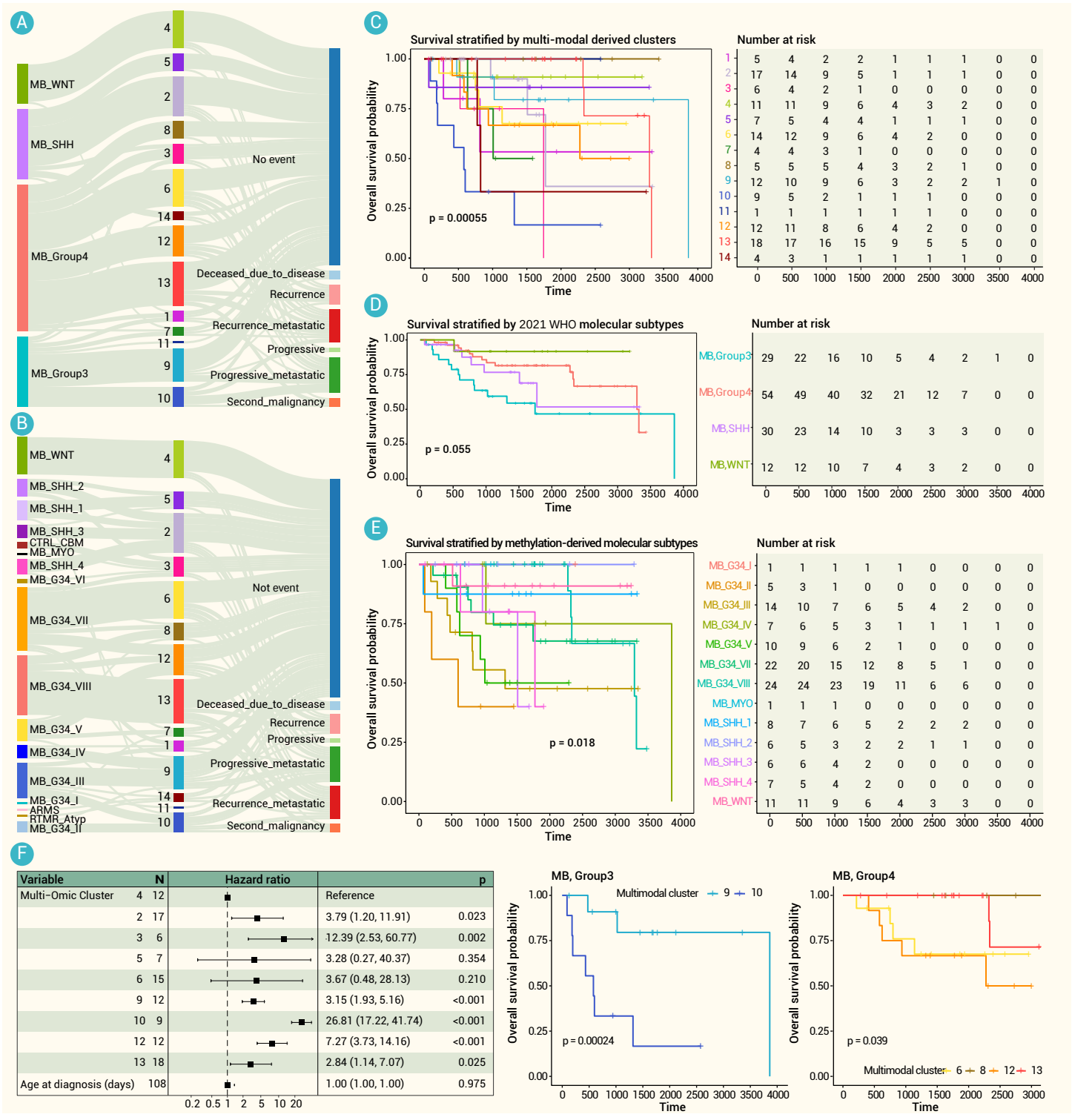

Figure 2. The relationship of MOCs with known subtypes and clinical outcomes (A) Relationship between WHO medulloblastoma classifications, novel MOC classifications, and clinical outcomes in the CBTN cohort. (B) Relationship between novel MOCs, second-generation DKFZ medulloblastoma subtype, and clinical outcomes in the CBTN cohort. Kaplan-Meier (KM) overall survival analysis of (C) MOCs, (D) WHO 2021 CNS Tumor Classifications, and (E) DKFZ classifications (p-value from log-rank test). (F) Results of a Cox regression analysis modeling OS as a function of MOC classification and age at diagnosis (variance adjusted for extent of tumor resection) and KM curves showing differences in G3/4 subclusters.

cycle control, were also important in the alternatively-spliced transcriptome in addition to metabolic and mitochondrial function (Table S5E).

Biological characterization of prognostically distinct G3 MOCs

Among prognostically distinct G3 MOCs, MOC9 (n=15), which combines DKFZ subtypes G3/4 III and IV, illustrated mutations in genes recurrently identified in G3 tumors involved in genomic instability and chromatin remodeling (*AHNAK2*, *PARP4*, *SMARCA4*, *KBTBD4*).[5] Further genomic alterations related to growth factor receptor signaling (*FGF1/10/13*, *TGFB3*) and immune/inflammatory signaling (*IL3/5/10*, *TNF*, *CD274*, *PDCD1LG2*; Figure 4B, Table S5) were identified. Further, 7 of 16 tumors showed losses in chr11 and gains in *BCL6*. At the transcriptional level, DEPs related to androgen receptor signaling, ribosomal RNA assembly, and DNA repair were upregulated relative to the rest of the tumor cohort, while pathways related to

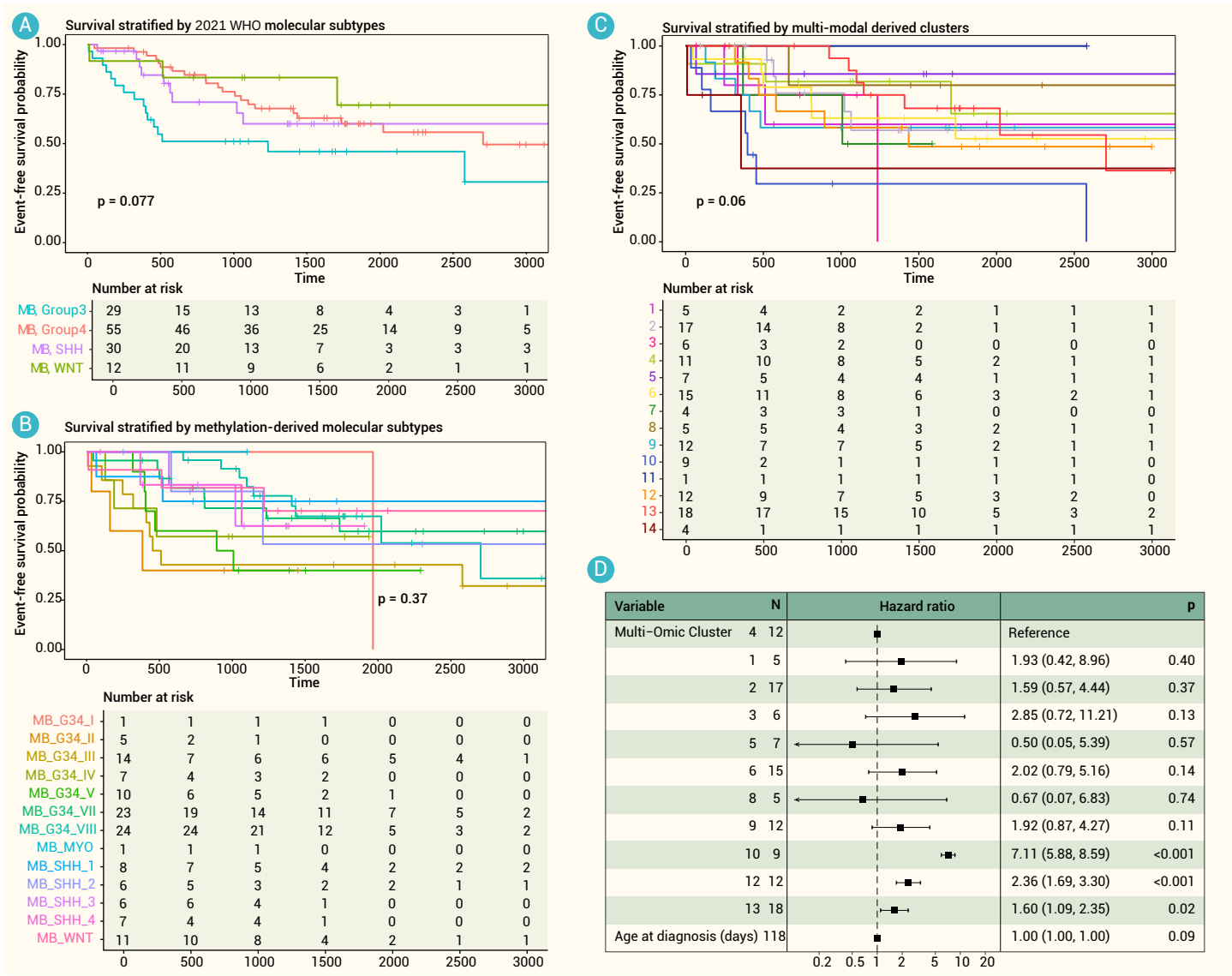

Figure 3. Assessment of event-free survival (EFS) characteristics on the basis of four-subtype, second-generation subtype, and MOC classifications (A) KM EFS curves for the CBTN cohort when annotated with the WHO 2021 CNS tumor classifications. (B) KM EFS analysis for the CBTN cohort when annotated with second-generation DKFZ subtypes. (C) KM EFS curves for the CBTN cohort when annotating tumors with MOC classifications. (D) KM EFS curves when annotating the CBTN cohort when second-generation Cavalli subtypes. (E) Results of a Cox regression analysis modeling EFS as a function of MOC classification and age at diagnosis (variance adjusted for extent of tumor resection).

ER stress, immunoregulatory signaling, and metabolic oxidations were down-regulated (Figure S3B). DMPs related to integrin-cell surface interactions, GPCR, and ECM remodeling were most prevalent (Figure S4B). When evaluating the alternatively-spliced transcriptome, proteostasis and organelle stress, RNA metabolism, and DNA repair, the latter identified in the genome and transcriptome, were enriched.

In prognostically poor MOC10 (n=9), which combines DKFZ groups G3/4_II and III, we observed recurrent mutations in cell cycle regulators and proliferation markers (*MYC, CDK5/7/18, MKI67, CCNE1/B1*), mitochondrial and metabolic genes, and genes involved in enhanced cell migration/invasion (*IL7/IL7R, CDH10, CDH20, VEGF*). Of note, *PLXNA2, ATAD3B, OVGP1, CASZ1, MKI67*, previously identified as recurrent in G3 tumors,[5] were also identified. MOC10 (n=9) also exhibited gains and amplifications in *PVT1* and *MYC* in 5 of 9 tumors (3 low-level gains, 2 amplifications), suggesting that *MYC* is not the sole determinant of OS in this cluster. DEPs included up-regulation of androgen receptor, beta catenin, Notch, and histone deacetylation (Figure S3C). The epigenome was characterized by changes in developmental, chemokine/cytokine, and GPCR signaling (Figure S4C), and the alternatively-spliced transcriptome consisted of biological mechanisms related to metabolic reprogramming (including *IDH2/3B*) and cell cycle/apoptotic pathways (Table S5E).

These findings provide evidence that multi-omic clustering identifies two potentially biologically distinct landscapes in G3 medulloblastoma, which may underpin their divergent clinical outcomes. MOC9 (n=16) represents a favorable-prognosis subset of tumors associated with the upregulation of DNA repair and proteostasis pathways alongside an epigenomic signature centered on ECM and integrin interactions. In contrast, MOC10 (n=9) exhibits evidence of a poor-prognosis, 'hyper-malignant' profile characterized by metabolic reprogramming, developmental Notch signaling, and enhanced cell migration that warrants further mechanistic investigation.

Characterization of G4 MOCs

Among intermediate-prognosis G4 tumors, MOC6 (n=17; DKFZ VII) exhibited SNV-indels involving RTK activity (*EGFR, MET*), MAPK/PI3K signaling, and inflammatory markers (Table S3), alongside recurrent G4 mutations (*KBTBD4, ZNF813*).[5] Transcriptomic and alternative splicing analyses revealed a metabolic shift toward starvation response and mitochondrial function (*IDH3B, NDUFS2*), coupled with intensive splicing regulation (*HNRNPM, SRSF10*; Figure S4D, Table S3E). MOC12 (n = 15), which represented a mixture of G3/4 DKFZ subtypes V, VII, and VIII, was associated with genomic alterations in immune modulation (*CD79B, JAK3*) and transcriptional co-regulation (*NCOR2, STAT5B*, Table S5A). MOC12 (n=15) was

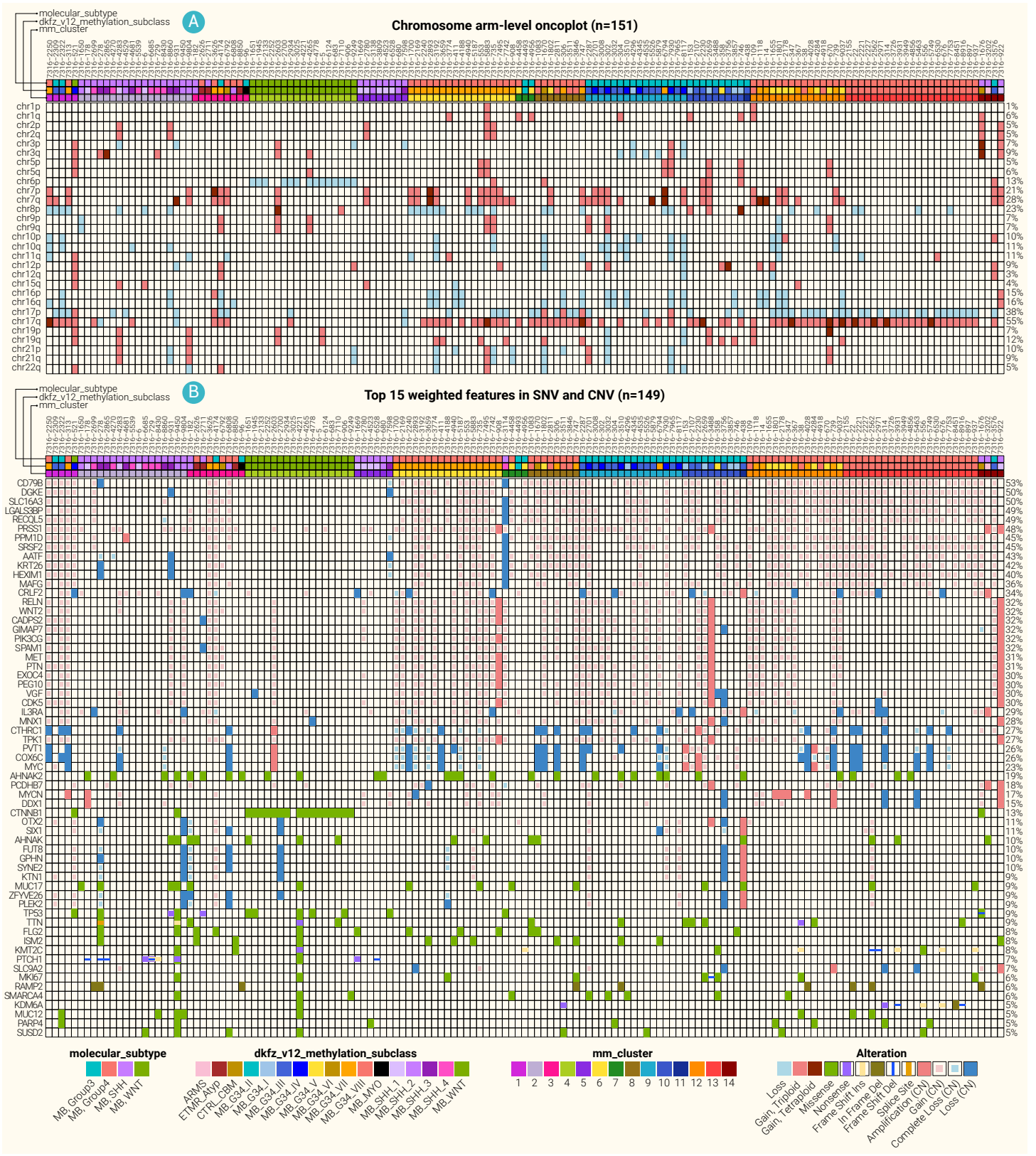

Figure 4. Somatic variation across medulloblastoma MOCs (A) Oncoplot of chromosomal arm-level copy number changes observed across CBTN medulloblastoma tumors. (B) Oncoplot of SNV/indel and CNVs observed across CBTN medulloblastoma tumors.

defined by SNV-indels involving immune modulation (*CD79B*, *JAK3*) and previously identified G4 alterations in *SOX1*, *MUC5AC*, *PARP4*, *STAG2*, *MEGF6*.[5] Further, notable CNVs were recurrently observed in *KDM6A* (3 deep deletions, 3 losses) and *CDK6* (8 gains; Tables S5A-B). Transcriptome analysis revealed suppressed pathways related to immune/inflammatory signaling (Figure S4E), and the alternatively-spliced transcriptome (Table S5E) revealed genes related to biological functions of ubiquitination, TGF-beta signaling (*TGFBR1*, *SMAD2*), tumor suppression (*PTEN*, *VHL*), and genome integrity (*ATRX, XPA, ERCC1*).

Prognostically favorable MOC8 (n = 8) contained DKFZ subtypes G3/4_V, VII, and VIII, with CNVs converging on the theme of DNA damage repair and epigenetic regulation (*KDM6B* [5 losses], *ZMYM3* [3 deep deletions, 2 losses],

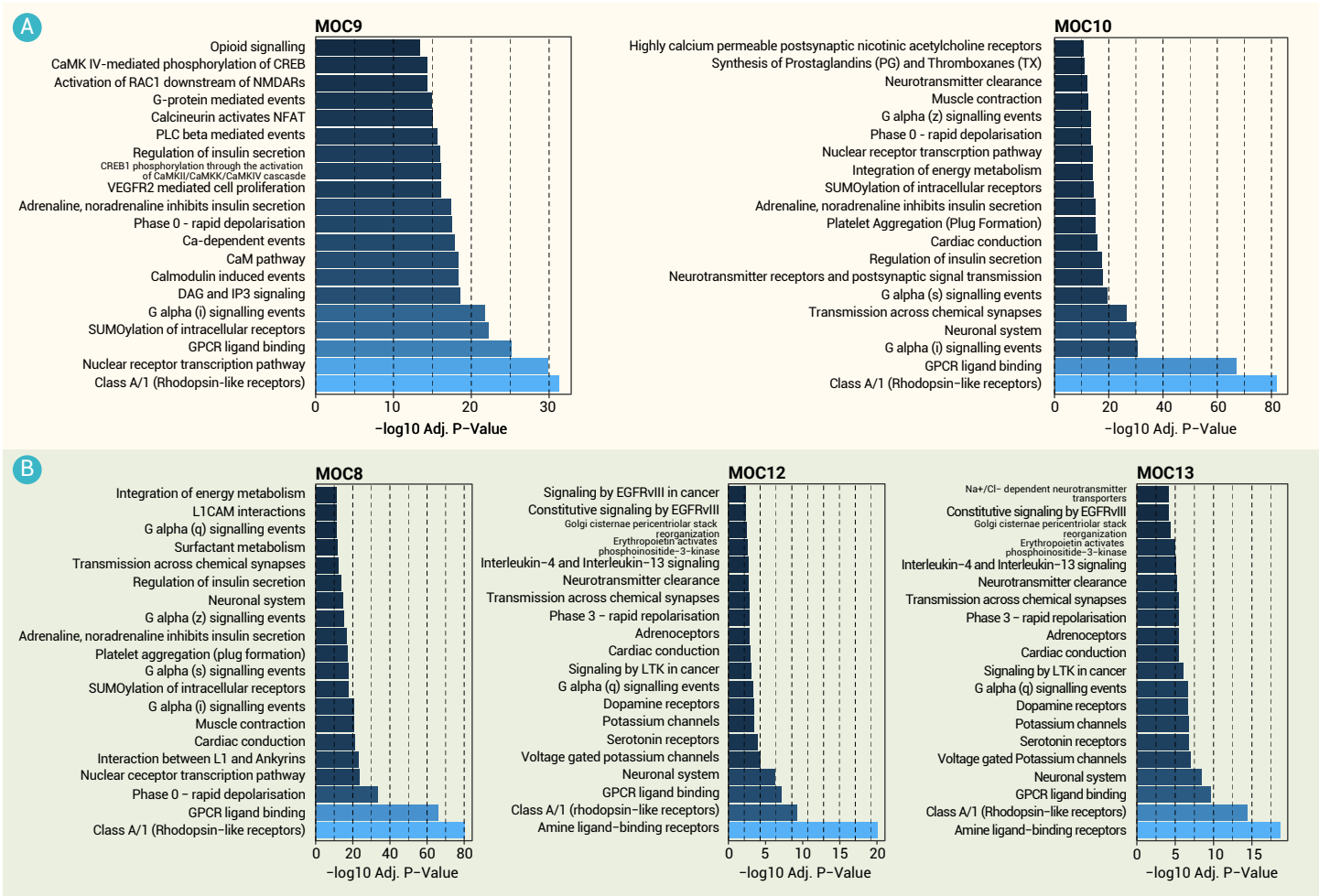

Figure 5. Cluster-specific transcriptomic characteristics across medulloblastoma MOCs (A) Target set enrichment analysis (TSEA) of significant LINCS chemical perturbagens (adjusted p-value <0.05 for connectivity analysis; reversers of disease phenotype only) comparing putative targetable Reactome pathways across G3 MOCs 9 and 10. (B) TSEA of significant LINCS chemical perturbagens (adjusted p-value <0.05 for connectivity analysis; reversers of disease phenotype only) comparing putative targetable Reactome pathways across G4 MOCs 8, 12, and 13 (no significant pathways in MOC 6).

MED12 [3 deep deletions, 2 losses], *BRCA2* [3 losses], and *ATM* [3 losses]). SNV-indel and CNV features also spanned across biological functions related to the cell cycle, transcriptional regulation, and cell adhesion (*PECAM1*, *VCAN*, *MUC17/4/16/12*, *LAMA5*, *CSPG4*, *COL1A1*, *CDH20*, *ICAM*). While DEPs largely overlapped with those of MOCs 6 and 12 (Figure S3F), the alternatively-spliced transcriptome was characterized by genes involved in oxidative stress balance and metabolic regulation (Table S5E). Prognostically favorable MOC13 (n = 21), a pure subset of G3/4_VIII, contained genomic features linked to development and oncogenesis including characteristic G4 mutations in *KMT2C*, *KDM6A*, *AHNAK2*, *MUC12*, and *ZMYM3*.[5] We also identified transcriptomic features largely overlapping with MOCs 6, 8, and 12 (Figure S3G), and a notable epigenomic pathway linked to SLC-mediated transmembrane transport (Figure S4D). The alternatively spliced transcriptome consisted of DNA repair and genome stability genes, mitotic genes, and genes related to ubiquitination and protein degradation (Table S5E).

These findings identify a previously unrecognized biological dichotomy: while intermediate-prognosis tumors are associated with a combination of RTK-mediated proliferation and metabolic reprogramming, favorable outcomes are associated with the maintenance of genome integrity and developmental homeostasis. By delineating these MOCs, we demonstrate that G4 outcomes may be rooted in fundamentally different biological dependencies.

Investigation of putative druggable pathways in MOCs

We aimed to infer differences in potential drug actionability by querying expression profiles against the Library of Integrated Network Cellular Signatures (LINCS),[20] focusing on prognostically distinct G3 (MOCs 9 and 10) and G4 (MOCs 6, 8, 12, 13) tumors. Target set enrichment analysis (TSEA) across G3 MOCs found that prognostically poor MOC10 (n=9) was distinguished from MOC9 (n=16) by nicotinic and acetylcholine, NCAM1, and insulin/energy metabolism pathways (Figure 5A, Table S6). When comparing prognostically favorable G4 tumors (MOCs 8 and 13, n=8 and n=21) to tumors of intermediate prognosis (MOCs 6 and 12, n=17 and n=15), we identified GPCR signaling as common, dominant features of both MOCs 8 and 13. Notably, STAT-FLT3 signaling was a recurrent and unique feature of MOC13 (Figure 5B). By contrast, MOC12 was characterized by recurrent enrichments in NOTCH, ERBB2, EGFR, ALK, and PI3K-Akt pathways, suggesting a highly distinct molecular profile that may harbor unique therapeutic vulnerabilities.

Prognostic splicing events highlight the functional role of splicing in G3/4 medulloblastoma MOCs

As aberrant splicing can drive medulloblastoma growth,[21] we utilized intNMF weights to identify functional markers of survival. We found eight splice events differing between MOC9 (n=16) and MOC10 (n=9). Intersecting these with G3-specific Cox regression results identified a single favorable event: increased exon inclusion in *SCAMP3* (Exon 2, chr1:155261656-155261734, PSI > 0.832; Figure S5A). This variant, which defines the favorable-risk MOC9 (n=16) but is absent in the poor-outcome MOC10 (n=9) (Figure 6A), encodes an EGFR-trafficking protein[22] and contained several predicted functional (from Uniprot) phosphorylation-binding sites, suggesting that exon inclusion may modulate *SCAMP3*'s signaling capacity and post-translational regulation (Figure 6B). Together, these findings highlight a prognostic role for *SCAMP3* splicing in medulloblastoma and emphasize the functional importance of splicing regulation in tumor biology.

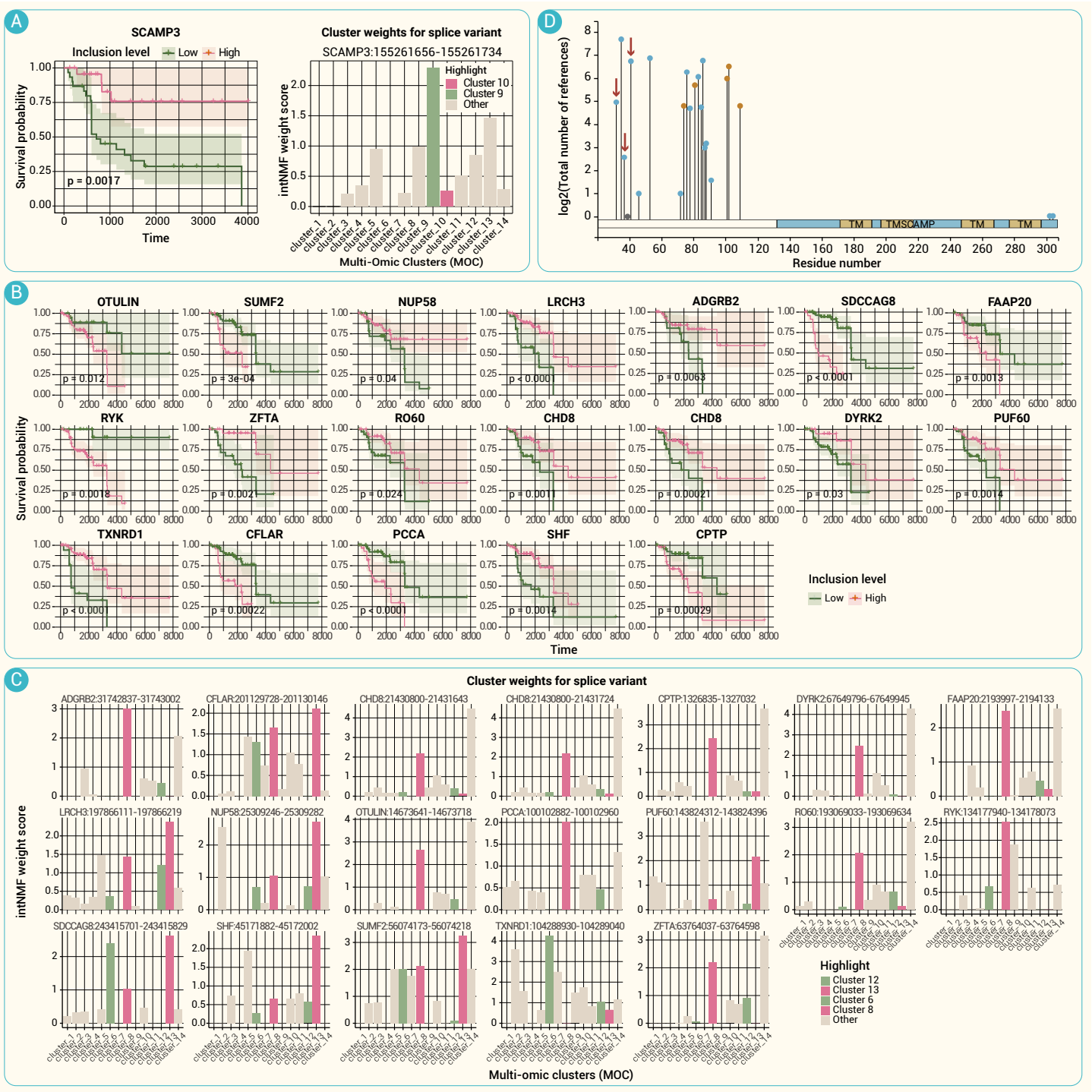

Figure 6. Prognostic differential splicing events identified across prognostically significant MOCs (A) Association of G3-specific differential splicing event in *SCAMP3* observed in MOCs 9 and 10 on OS. Bar chart illustrates differences in intNMF weights across MOCs B) PhosphositePlus protein visual highlighting predicted impact of *SCAMP3* splicing event on phosphorylation binding sites (Uniprot-defined annotations highlighted with arrows). C) Predicted prognostic (OS) differential splicing events in G4 MOC's 6, 8, 12 and 13. D) intNMF weights illustrating G4-specific splicing events.

To identify G4 prognostic markers, we compared poorer-outcome MOCs 6 (n=17) and 12 (n=15) against favorable MOCs 8 (n=8) and 13 (n=21). Leveraging differential inclusion in favorable clusters, we identified 19 OS-associated splice events (Figures 6C-D). Except for *TXNRD1*, all exhibited higher intNMF weights and exon inclusion (PSI) in MOCs 8/13, correlating with improved survival (Figure 6D). Notably, nine variants met both criteria, of which several are established tumor suppressors (*ADGRB2*, *CHD8*, *DYRK2*, *PUF60*, *SHF*) or fusion-related genes involved in pediatric cancer development (*LRCH3*, *ZFTA*, Figures 6C-D).[23-29] These findings suggest that splicing disruption impacts medulloblastoma risk through the loss of tumor-suppressive isoforms.

Investigation of putative regulatory methylation sites in prognostically significant MOCs

To further understand biological mechanisms at play in the MOCs, we aimed to identify putative regulatory methylation sites, defined as sites mapping to promoters uniquely hyper- or hypo-methylated in an MOC relative to GTEx normal methylation levels and that influence expression of the target gene (Figures S5-S7).

Among the top events we observed in prognostically favorable G3 MOC9 (n=16), we observed a promoter hypermethylation in the Rho GDP dissociation inhibitor encoded by *ARHGDIB* (Figure S6), a biomarker of outcome in bladder cancer.[30] We also observed hypermethylation of the phosphodi-

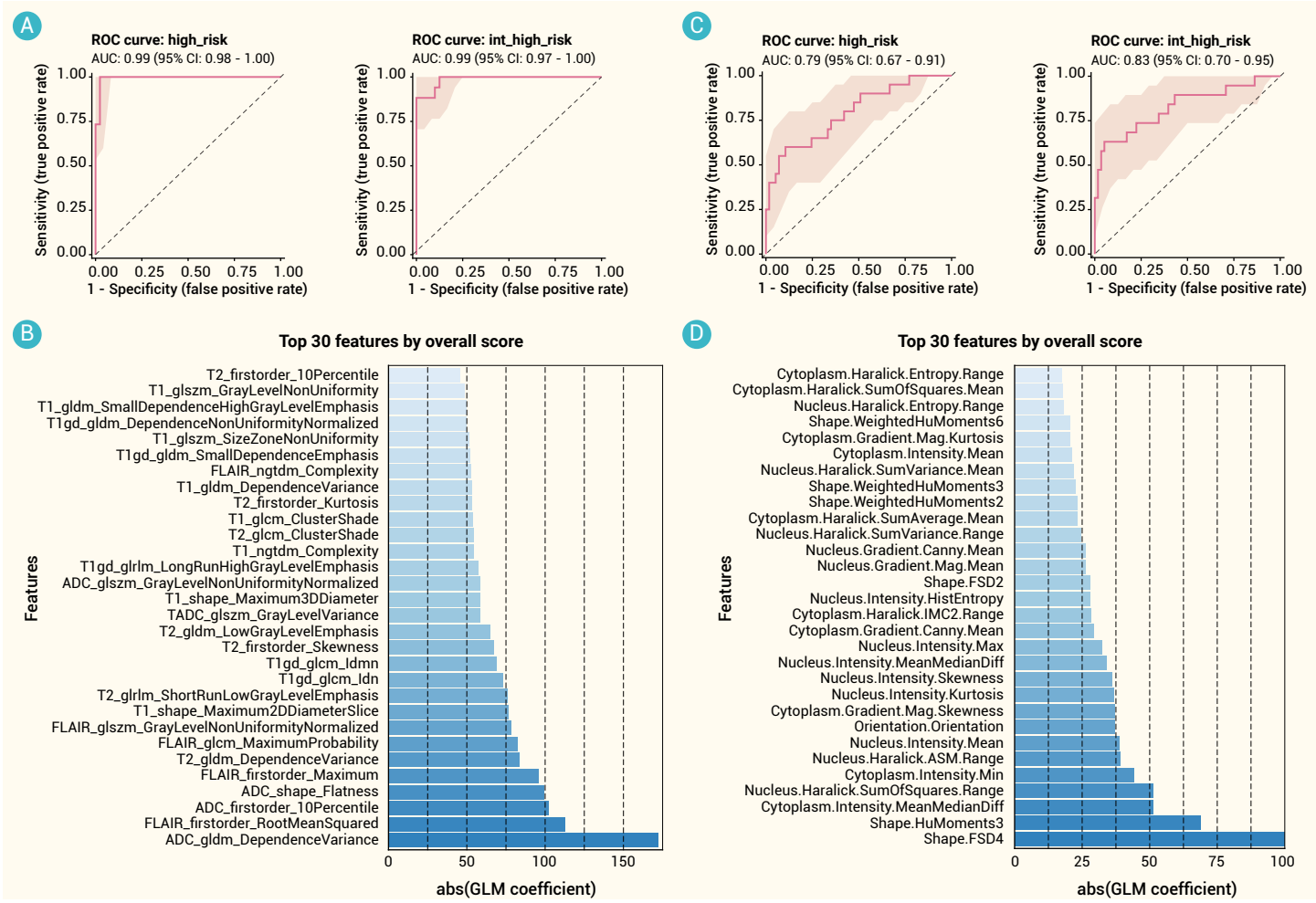

Figure 7. Elastic net logistic regression of MOC-based risk as a function of pre-operative MRI and pathomic features (A) ROC curves illustrating the true and false positive rates for predicting intermediate-high and high-risk groups (from upper risk quartiles of MOC-based Cox regression, Figure 2, OS endpoint) from MRI features. (B) Standardized GLM coefficients of the 30 most heavily weighted MRI features from elastic net multinomial logistic regression found to be predictive of MOC-defined risk. (C) ROC curves illustrating the true and false positive rates for predicting intermediate-high and high risk groups risk groups (from upper risk quartiles of MOC-based Cox regression, Figure 2, EFS endpoint) from pathology-based imaging features. (D) Standardized GLM coefficients of the 30 most heavily weighted pathology-based imaging features found to be predictive of MOC-defined risk.

esterase 2A *PDE2A* (Figure S5), a known prognostic marker for hepatocellular carcinoma.[31] We also observed hypermethylation in the cyclin dependent kinase inhibitor *CDKN1A*, a known marker of cancer development (Figure S5).[32,33] In prognostically unfavorable G3 MOC10 (n=9), we observed promoter hypermethylation in the secreted frizzled-related protein *SERP2*, a recognized WNT-related marker of poor outcome in adult cancers[34,35] (Figure S6). We also observed hypermethylation of *SKI* and *ABHD6*, both of which play tumor suppressive roles by inhibiting TGF-β1/Smad signaling in the case of *SKI* and AKT signaling in the case of *ABHD6*.[36-38] MOC10 (n=9) also exhibited hypomethylation of the central transmembrane component of the Hedgehog pathway *PTCH1*, and hypomethylation at this locus has been observed to promote rhabdomyosarcoma formation[39] (Figure S6). Known cancer associated methylation events in prognostically unfavorable G4 MOCs 6 (n=17) and 12 (n=15) harbored events included hypermethylation of *GLT8D2* (gastric cancer[40]), *ERG* (prostate cancer[41]), and *SYK* (gastric, breast, and bladder carcinomas[42,43]), *KLF9* (glioma[44]) (Figure S7).

Taken together, these epigenetic profiles reveal that MOC-specific outcomes may be driven by a distinct regulatory logic where the aggressive phenotype of MOC10 may be due to the silencing of tumor-suppressive axes, such as TGFB/Smad and AKT inhibition. Parallel to this, our analysis suggests a previously undescribed regulatory architecture in G4, where intermediate-prognosis MOCs leverage hyper-methylated signatures to suppress lineage-differentiation programs via genes like *KLF9* and *ERG*.

Potential for MR and pathology-based imaging data to predict MOC-based medulloblastoma risk groups

We sought to determine whether foundational data routinely generated in the clinic, namely pathology and MR imaging, have the potential to predict risk defined by multi-omic clustering. Given the limited availability of shared data across modalities (multi-omic + pathomic, n = 77; multi-omic + MRI, n = 57), we reclassified tumors into four major risk subgroups (low, intermediate-low, intermediate-high, high) using the quartiles of computed risk scores from the MOC-based Cox regression analysis for OS and EFS (Figure 2F). Elastic net logistic regression using radiomics features predicted intermediate-high and high-risk tumors with AUROCs of 0.99 (95% CI: 0.97 - 1, 95% CI: 0.98 - 1) (Figure 7A). Texture-based metrics from ADC and FLAIR sequences emerged as the primary predictors (Figure 7B, Table S7A). ADC features likely capture variations in tumor cellularity and water diffusion restriction, whereas FLAIR features reflect heterogeneity in peritumoral edema and non-enhancing tumor components associated with recurrence.

Pathomic analysis using EFS as the endpoint yielded AUROCs of 0.83 (95% CI: 0.7 - 0.95) and 0.79 (95% CI: 0.67 – 91) for intermediate-high and high risk groups, respectively, when leveraging an elastic net logistic regression model (Figure 7C). Predictive features included nuclear and cytoplasmic intensity, shape, and texture (Figure 7D, Table S7B). Specifically, asymmetry in intensity distributions (kurtosis, entropy) and Haralick texture variance highlighted chromatin irregularity and cytoplasmic disorganization. These markers likely differentiate the hypochromatic, pleomorphic nature of high-risk histologies

(e.g., LCA, desmoplastic/nodular) from the uniform, undifferentiated nuclei of lower-risk (classic) tumors. Furthermore, nuclear shape features, including Fourier descriptors (FSD4, FSD2) and Hu moments, captured structural deformations and edge periodicity. These reflect the characteristic elongation and shape heterogeneity (pleomorphism) that distinguish high-risk subgroups from more circular, classic nuclear morphologies.

While based on a limited cohort, these findings demonstrate that quantitative features derived from standard clinical imaging and pathology correlate with MOC-defined risk. Such associations serve as a preliminary proof of concept regarding the feasibility of leveraging phenotypic markers, such as nuclear deformation and ADC-based cellularity metrics, to identify high-risk molecular profiles when comprehensive genomic profiling is unavailable.

DISCUSSION

Our study demonstrates that integrating five molecular layers, including the dimension of alternative splicing, resolves latent biological heterogeneity in medulloblastoma that remains obscured by traditional transcriptomic or epigenetic profiling alone. By identifying 14 MOCs, we provide a framework that not only refines prognostic stratification but also nominates specific biological dependencies for precision intervention.[1,5,7] To maximize the clinical utility of the MOCs in routine practice, we propose contextualizing these MOCs within established diagnostic frameworks, specifically focusing on WHO G3 and G4, where we observe the most divergent outcomes between clusters. Because clinicians already rely on baseline WHO subgroup assignments, the MOC framework can serve as a critical secondary stratification tool to guide patient-specific therapeutic modifications. For instance, for a patient with aggressive G3 medulloblastoma who has completed standard therapy, determining whether their tumor aligns with MOC9 versus MOC10 could inform a decision regarding whether to pursue additional maintenance therapy. By narrowing the clinical focus to these highly actionable intra-subgroup disparities, this approach allows oncologists to translate high-dimensional molecular data into immediate, individualized treatment decisions.

The refined prognostic resolution of G3/4 tumors carries significant implications for the next generation of precision medicine. Historically, these non-WNT/non-SHH tumors have been treated as relatively broad entities with unpredictable clinical trajectories. By disambiguating "hyper-malignant" states from favorable-prognosis clusters, our model provides a biological rationale for therapeutic stratification. For G3 patients, identifying the metabolic and Notch-signaling shifts in MOC10 allows for the potential intensification of therapy or the introduction of targeted inhibitors,[45-47] whereas patients in the genomic-maintenance state of MOC9 may eventually be candidates for de-escalation to reduce long-term sequelae.[6] Furthermore, the discovery that G4 outcomes are rooted in divergent dependencies such as RTK-mediated proliferation in MOC12 versus FLT3-STAT5 signaling in MOC13 suggests that novel therapeutic development for non-WNT tumors without cohort enrichment can only be, at best, partially successful.[48,49] Instead, these clusters nominate distinct, actionable pathways that could be leveraged for combination therapies tailored to the tumor's specific multi-omic signature.[3]

A key novelty of this framework is the integration of alternative splicing. By identifying prognostically significant splicing events, we go beyond mRNA abundance to capture structural transcript diversity that influences tumor phenotype. These findings suggest that splicing-derived biomarkers may offer a more nuanced lens for risk-stratification and the discovery of novel neoantigens or functional isoforms, which are critical for the development of immunotherapy and RNA-based precision medicines.[1]

To address the barrier of global accessibility, we evaluated routinely generated MRI and H&E histopathology as surrogates for molecular risk. While these findings are exploratory and were based on repartitioning our dataset into MOC-defined risk quartiles in lieu of predicting MOC assignment directly, the ability of imaging features to predict high-risk MOCs suggests a path toward equitable precision medicine. Such tools could provide rapid, cost-effective biological stratification in resource-limited settings where comprehensive sequencing is unavailable.[4]

Despite the strength of this CBTN multi-modal cohort being the largest known with multi-omic and imaging data, we acknowledge limitations, including the need for validation in uniform clinical trial cohorts to ensure prognostic signatures are independent of treatment variability. Future efforts will focus on expanding imaging data with CBTN partner institutions to enable the direct prediction of MOC classifications. Further, while we aimed to adjust for all established prognostic factors in our Cox regression models, the inclusion of treatment variables (chemotherapy, metastasis, and radiation) resulted in model non-convergence, likely due to event rates in certain multi-omic clusters. Consequently, our multivariable models are primarily limited to adjusting for age and extent of resection. Therefore, the prognostic value of our MOC framework must be validated in future, statistically powered studies utilizing cohorts with complete metastatic staging and known treatment protocols.

CONCLUSION

In conclusion, five data-layer integration offers a significant advancement in defining medulloblastoma substructure, providing a roadmap to guide biology-specific combination therapies and mitigate the lifelong burden of standard-of-care treatments.

REFERENCES

1. Northcott P.A., Buchhalter I., Morrissy A.S., et al. (2017). The whole-genome landscape of medulloblastoma subtypes. *Nature* **547**:311–317. DOI:10.1038/nature22973
2. Coltin H., Pequeno P., Liu N., et al. (2023). The Burden of surviving childhood medulloblastoma: A population-based, matched cohort study in Ontario, Canada. *J. Clin. Oncol.* **41**:2372–2381. DOI:10.1200/JCO.22.02466
3. Cavalli F.M., Remke M., Rampasek L., et al. (2017). Intertumoral heterogeneity within medulloblastoma subgroups. *Cancer Cell* **31**:737–754.e736. DOI:10.1016/j.ccell.2017.05.005
4. Louis D.N., Perry A., Wesseling P., et al. (2021). The 2021 WHO classification of tumors of the central nervous system: A summary. *Neuro. Oncol.* **23**:1231–1251. DOI:10.1093/neuonc/noab106
5. Sharma T., Schwalbe E.C., Williamson D., et al. (2019). Second-generation molecular subgrouping of medulloblastoma: An international meta-analysis of Group 3 and Group 4 subtypes. *Acta Neuropathol.* **138**:309–326. DOI:10.1007/s00401-019-02020-0
6. Smith K.S., Dhanda S.K., Billups C.A., et al. (2025). An integrated analysis of three medulloblastoma clinical trials refines risk-stratification approaches for reducing toxicity and improving survival. *Neuro. Oncol.* **28**:268–281. DOI:10.1093/neuonc/noaf250
7. Kumar R., Smith K.S., Deng M., et al. (2021). Clinical outcomes and patient-matched molecular composition of relapsed medulloblastoma. *J. Clin. Oncol.* **39**:807–821. DOI:10.1200/JCO.20.01359
8. Chalise P. and Fridley B.L. (2017). Integrative clustering of multi-level 'omic data based on non-negative matrix factorization algorithm. *PLoS One* **12**:e0176278. DOI:10.1371/journal.pone.0176278
9. Capper D., Jones D.T.W., Sill M., et al. (2018). DNA methylation-based classification of central nervous system tumours. *Nature* **555**:469–474. DOI:10.1038/nature26000
10. Silva T.C., Young J.I., Martin E.R., et al. (2022). MethReg: Estimating the regulatory potential of DNA methylation in gene transcription. *Nucleic Acids Res.* **50**:e51. DOI:10.1093/nar/gkac030
11. Juraschka K. and Taylor M.D. (2019). Medulloblastoma in the age of molecular subgroups: A review. *J. Neurosurg. Pediatr.* **24**:353–363. DOI:10.3171/2019.5.PEDS18381
12. Zou H., Poore B., Broniscer A., et al. (2020). Molecular heterogeneity and cellular diversity: Implications for precision treatment in medulloblastoma. *Cancers (Basel)* **12**. DOI:10.3390/cancers12030643.
13. Tavtigian S.V., Harrison S.M., Boucher K.M., et al. (2020). Fitting a naturally scaled point system to the ACMG/AMP variant classification guidelines. *Hum. Mutat.* **41**:1734–1737. DOI:10.1002/humu.24088
14. Richards S., Aziz N., Bale S., et al. (2015). Standards and guidelines for the interpretation of sequence variants: A joint consensus recommendation of the American College of Medical Genetics and Genomics and the Association for Molecular Pathology. *Genet. Med.* **17**:405–424. DOI:10.1038/gim.2015.30
15. Northcott P.A., Korshunov A., Witt H., et al. (2011). Medulloblastoma comprises four distinct molecular variants. *J. Clin. Oncol.* **29**:1408–1414. DOI:10.1200/JCO.2009.27.4324
16. Northcott P.A., Shih D.J., Peacock J., et al. (2012). Subgroup-specific structural variation across 1,000 medulloblastoma genomes. *Nature* **488**:49–56. DOI:10.1038/nature11327
17. Lui V.W., Hedberg M.L., Li H., et al. (2013). Frequent mutation of the PI3K pathway in head and neck cancer defines predictive biomarkers. *Cancer Discov.* **3**:761–769. DOI:10.1158/2159-8290.CD-13-0103
18. Sikkema A.H., den Dunnen W.F., Hulleman E., et al. (2012). EphB2 activity plays a pivotal role in pediatric medulloblastoma cell adhesion and invasion. *Neuro. Oncol.*

14:1125–1135. DOI:10.1093/neuonc/nos130
19. Jing H., Hu J., He B., et al. (2016). A SIRT2-Selective inhibitor promotes c-Myc oncoprotein degradation and exhibits broad anticancer activity. *Cancer Cell* **29**:297–310. DOI:10.1016/j.ccell.2016.02.007
20. Keenan A.B., Jenkins S.L., Jagodnik K.M., et al. (2018). The library of integrated network-based cellular signatures NIH program: System-level cataloging of human cells response to perturbations. *Cell Syst.* **6**:13–24. DOI:10.1016/j.cels.2017.11.001
21. Ouyang J., Zhang Y., Xiong F., et al. (2021). The role of alternative splicing in human cancer progression. *Am. J. Cancer Res.* **11**:4642–4667. DOI:10.21236/ada477527
22. Acevedo-Diaz A., Morales-Caban B.M., Zayas-Santiago A., et al. (2022). SCAMP3 regulates EGFR and promotes proliferation and migration of triple-negative breast cancer cells through the modulation of AKT, ERK, and STAT3 signaling pathways. *Cancers (Basel)* **14**:2807. DOI:10.3390/cancers14112807
23. Kumamoto T., Yamada K., Yoshida S., et al. (2020). Impairment of DYRK2 by DNMT1-mediated transcription augments carcinogenesis in human colorectal cancer. *Int. J. Oncol.* **56**:1529–1539. DOI:10.3892/ijo.2020.5020
24. Gad A.A. and Balenga N. (2020). The emerging role of adhesion GPCRs in cancer. *ACS Pharmacol. Transl. Sci.* **3**:29–42. DOI:10.1021/acsptsci.9b00093
25. Chase A., Ernst T., Fiebig A., et al. (2010). TFG, a target of chromosome translocations in lymphoma and soft tissue tumors, fuses to GPR128 in healthy individuals. *Haematologica* **95**:20–26. DOI:10.3324/haematol.2009.011536
26. Sawada G., Ueo H., Matsumura T., et al. (2013). CHD8 is an independent prognostic indicator that regulates Wnt/beta-catenin signaling and the cell cycle in gastric cancer. *Oncol. Rep.* **30**:1137–1142. DOI:10.3892/or.2013.2597
27. Zhang C., Ni X., Tao C., et al. (2024). Targeting PUF60 prevents tumor progression by retarding mRNA decay of oxidative phosphorylation in ovarian cancer. *Cell. Oncol. (Dordr)* **47**:157–174. DOI:10.1007/s13402-023-00859-w
28. Wang J., Huang Z., Ji L., et al. (2022). SHF acts as a novel tumor suppressor in glioblastoma multiforme by disrupting STAT3 dimerization. *Adv. Sci. (Weinh)* **9**:e2200169. DOI:10.1002/advs.202200169
29. Pages M., Pajtler K.W., Puget S., et al. (2019). Diagnostics of pediatric supratentorial RELA ependymomas: Integration of information from histopathology, genetics, DNA methylation and imaging. *Brain. Pathol.* **29**:325–335. DOI:10.1111/bpa.12664
30. Liu L., Cui J., Zhao Y., et al. (2021). KDM6A-ARHGDIB axis blocks metastasis of bladder cancer by inhibiting Rac1. *Mol. Cancer* **20**:77. DOI:10.1186/s12943-021-01369-9
31. Chen L., Zhou J., Zhao Z., et al. (2022). Low expression of phosphodiesterase 2 (PDE2A) promotes the progression by regulating mitochondrial morphology and ATP content and predicts poor prognosis in hepatocellular carcinoma. *Cells* **12**:68. DOI:10.3390/cells12010068
32. Manousakis E., Miralles C.M., Esquerda M.G., et al. (2023). CDKN1A/p21 in breast cancer: Part of the problem, or part of the solution? *Int. J. Mol. Sci.* **24**:17488. DOI:10.3390/ijms242417488
33. Watanabe M., Nakahata S., Hamasaki M., et al. (2010). Downregulation of CDKN1A in adult T-cell leukemia/lymphoma despite overexpression of CDKN1A in human T-lymphotropic virus 1-infected cell lines. *J. Virol.* **84**:6966–6977. DOI:10.1128/JVI.00073-10
34. Yu J., Xie Y., Li M., et al. (2019). Association between SFRP promoter hypermethylation and different types of cancer: A systematic review and meta-analysis. *Oncol. Lett.* **18**:3481–3492. DOI:10.3892/ol.2019.10709
35. Chen Y.Z., Liu D., Zhao Y.X., et al. (2014). Aberrant promoter methylation of the SFRP1 gene may contribute to colorectal carcinogenesis: A meta-analysis. *Tumour Biol.* **35**:9201–9210. DOI:10.1007/s13277-014-2180-x
36. Xie M., Wu X., Zhang J., et al. (2017). Ski regulates Smads and TAZ signaling to suppress lung cancer progression. *Mol. Carcinog.* **56**:2178–2189. DOI:10.1002/mc.22661
37. Deheuninck J. and Luo K. (2009). Ski and SnoN, potent negative regulators of TGF-beta signaling. *Cell Res.* **19**:47–57. DOI:10.1038/cr.2008.324
38. Xiong X., Yang C., Jin Y., et al. (2024). ABHD6 suppresses colorectal cancer progression via AKT signaling pathway. *Mol. Carcinog.* **63**:647–662. DOI:10.1002/mc.23678
39. Nitzki F., Tolosa E.J., Cuvelier N., et al. (2015). Overexpression of mutant Ptch in rhabdomyosarcomas is associated with promoter hypomethylation and increased Gli1 and H3K4me3 occupancy. *Oncotarget* **6**:9113–9124. DOI:10.18632/oncotarget.3272
40. Xu H., Huang K., Lin Y., et al. (2023). Glycosyltransferase GLT8D1 and GLT8D2 serve as potential prognostic biomarkers correlated with tumor immunity in gastric cancer. *BMC Med. Genomics* **16**:123. DOI:10.1186/s12920-023-01559-y
41. Schwartzman J., Mongoue-Tchokote S., Gibbs A., et al. (2011). A DNA methylation microarray-based study identifies ERG as a gene commonly methylated in prostate cancer. *Epigenetics* **6**:1248–1256. DOI:10.4161/epi.6.10.17727
42. Wang S., Ding Y.B., Chen G.Y., et al. (2004). Hypermethylation of Syk gene in promoter region associated with oncogenesis and metastasis of gastric carcinoma. *World J. Gastroenterol.* **10**:1815–1818. DOI:10.3748/wjg.v10.i12.1815
43. Kunze E., Wendt M. and Schlott T. (2006). Promoter hypermethylation of the 14-3-3 σ, SYK and CAGE-1 genes is related to the various phenotypes of urinary bladder carcinomas and associated with progression of transitional cell carcinomas. *Int. J. Mol. Med.* **18**:547–557. DOI:10.3892/ijmm.18.4.547
44. Huang S., Wang C., Yi Y., et al. (2015). Kruppel-like factor 9 inhibits glioma cell proliferation and tumorigenicity via downregulation of miR-21. *Cancer Lett.* **356**:547–555. DOI:10.1016/j.canlet.2014.10.007
45. Pham K., Maxwell M.J., Sweeney H., et al. (2021). Novel glutamine antagonist JHU395 suppresses MYC-driven medulloblastoma growth and induces apoptosis. *J. Neuropathol. Exp. Neurol.* **80**:336–344. DOI:10.1093/jnen/nlab018
46. Takebe N., Miele L., Harris P.J., et al. (2015). Targeting Notch, Hedgehog, and Wnt pathways in cancer stem cells: Clinical update. *Nat. Rev. Clin. Oncol.* **12**:445–464. DOI:10.1038/nrclinonc.2015.61
47. Gwynne W.D., Suk Y., Custers S., et al. (2022). Cancer-selective metabolic vulnerabilities in MYC-amplified medulloblastoma. *Cancer Cell* **40**:1488–1502.e1487. DOI:10.1016/j.ccell.2022.10.009
48. Karaulic A., Fournier C. and Pages G. (2025). Exploring novel applications: Repositioning clinically approved therapies for medulloblastoma treatment. *Cancers (Basel)* **17**. DOI:10.3390/cancers17223659
49. Xiao H., Bid H.K., Jou D., et al. (2015). A novel small molecular STAT3 inhibitor, LY5, inhibits cell viability, cell migration, and angiogenesis in medulloblastoma cells. *J. Biol. Chem.* **290**:3418–3429. DOI:10.1074/jbc.M114.616748

FUNDING AND ACKNOWLEDGMENTS

Research reported in this publication was supported by the Gabriella Miller Kids First Pediatric Research Program of the National Institutes of Health under Award Number U2CHD109731. The authors would like to acknowledge Phillip Duarte, Andrew Wang, and Arman Nejati for their assistance in preparing the pathology imaging dataset. The authors wish to thank the anonymous private investors to the Children's National Hospital Brain Tumor Institute who have supported this work. The funders had no role in study design, data collection and analysis, decision to publish, or preparation of the manuscript.

AUTHOR CONTRIBUTIONS

AK, ACR, and BR conceived and designed the study. PJS generated biospecimens from neurosurgery. AK, KR, VK, YG, QL, YZ, XH, BZ, and ASN analyzed, generated, and/or interpreted molecular data from the study. AK, AFK, AMF, ANV, MS, DG, AV, and AN analyzed, generated, and/or interpreted imaging data from the study. All authors contributed to the manuscript and approved the final version.

DECLARATION OF INTERESTS

Dr. Arastoo Vossough reports serving as an advisor for DeepSight and as a consultant for Syneos. The remaining authors declare no competing interests.

ETHICAL STATEMENT AND PATIENT CONSENT

This study utilized retrospectively collected data from the Children's Brain Tumor Network (CBTN) repository (cbtn.org), a biorepository of de-identified clinical, imaging, and biospecimen data for research. The study was conducted in compliance with HIPAA regulations and received Institutional Review Board (IRB) approval from the Children's Hospital of Philadelphia (CHOP) under the CBTN protocol (Approval Number IRB 09-007316), with informed consent obtained for patient participation.

DATA AND CODE AVAILABILITY

De-identified genomic, transcriptomic, and clinical data, including patient baseline characteristics, molecular subtypes, and outcomes, were obtained from publicly available resources. These datasets can be accessed through the dbGaP study under accession number phs002517.v4.p2 [https://www.ncbi.nlm.nih.gov/projects/gap/cgi-bin/study.cgi?study_id=phs002517] and the KidsFirst Data Resource Portal (https://kidsfirstdrc.org/) under study ID phs002517.

SUPPLEMENTAL INFORMATION

It can be found online at https://doi.org/10.59717/j.xinn-oncol.2026.100025